Slenderness effects in thin-walled I-section struts susceptible to local–global mode interaction

Li Bai[a,b,c,], M. Ahmer Wadee[c,*]

[a] *State Key Laboratory of Ocean Engineering, School of Naval Architecture, Ocean and Civil Engineering, Shanghai Jiao Tong University, Shanghai 200240, P. R. China*
[b] *Collaborative Innovation Center for Advanced Ship and Deep-Sea Exploration (CISSE), Shanghai 200240, P. R. China*
[c] *Department of Civil and Environmental Engineering, Imperial College London, South Kensington Campus, London SW7 2AZ, UK*

Abstract

A variational model that describes the nonlinear interaction between the global and local buckling of a thin-walled I-section strut under pure compression is presented and subsequently exploited. A parametric study is conducted for two limiting cases, where the flange–web joint is assumed to be pinned or rigid. For a chosen set of geometries, the most undesirable parametric spaces are identified for both global and local slendernesses, in terms of the strut length and the flange width respectively, where highly unstable behaviour is observed in the post-buckling range. Practical implications are discussed in terms of the idealized design strength relationship.

Keywords: Mode interaction; Global buckling; Local buckling; Cellular buckling; Nonlinear mechanics.

1. Introduction

Structural members made from slender plate elements entirely under compression, or in part, are well known to be susceptible to a variety of different elastic instability phenomena [1, 2, 3, 4, 5, 6, 7, 8, 9, 10]. In recent works [11, 12], a variational model representing an open and doubly-symmetric thin-walled I-section strut under axial compression, made from a linear elastic material, was introduced where both local or global buckling could occur first. Numerical examples, focusing on the cases where the interaction between the global buckling mode about the weak axis of bending and the local buckling modes was most likely to take place, revealed conditions where highly unstable cellular [13] and non-cellular post-buckling behaviour would be expected. The results from the analytical model showed good comparisons against experiments from the literature [14] and recently

*Corresponding author

Email addresses: `li.bai06@imperial.ac.uk` (Li Bai), `a.wadee@imperial.ac.uk` (M. Ahmer Wadee)

developed finite element models [12], hence validating the approach. Moreover, it was found by van der Neut [15, 16], while studying an idealized model of a strut, that the post-buckling behaviour may be approximately neutral, strongly stable or strongly unstable if the strut length is varied, assuming that all other cross-section properties remain constant, as shown in Figure 1. It is therefore expected that with varying geometric properties, the

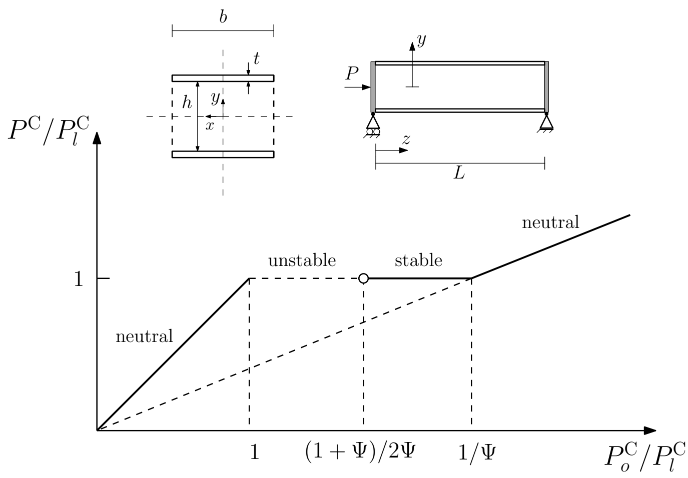

Figure 1: The van der Neut strut and graph [15]. The strut comprises two load carrying flanges with width b, thickness t, length L with two webs of depth h being laterally rigid with no longitudinal stiffness; Ψ is the stiffness reduction factor; P is the applied compressive force on the entire strut with P^{C}, P_o^{C} and P_l^{C} being the critical, the global and the local buckling loads respectively. In this case, the strut length L reduces as $P_o^{\mathrm{C}}/P_l^{\mathrm{C}}$ increases.

corresponding variation in global and local slendernesses would result in different post-buckling behaviour, which needs to be investigated in detail such that the actual load carrying capacity may be predicted with confidence.

A parametric investigation, to determine the effect of varying both global and local slendernesses, is conducted by studying the governing nonlinear system of equations using the numerical continuation package Auto [17]. The variation in the global and the local slendernesses is achieved by varying the strut length and the width of the flange plates respectively. The present work focuses on the cases where the flange–web joint is assumed to be pinned or rigid, the boundary conditions for which the behaviour of the local buckling of the flange plates is well understood [18]. Both cases where global buckling or local buckling being critical can be studied with the present analytical model. It is confirmed that when the local buckling load is significantly higher than the global buckling load, global buckling about the weak axis is dominant; conversely when the global buckling load is significantly higher than the local buckling load, the opposite is true. Under such conditions, there is practically no interaction between the global and the local buckling modes. However, within a defined interactive region, it is found that the strut exhibits post-buckling equilibrium paths with distinctive characteristics, including cellular buckling, which are highlighted and discussed presently. It should be stressed that all the computations are performed for purely elastic systems and that any plasticity effects would change the results albeit only marginally for the geometries studied.

2. Analytical model development

Consider a simply-supported thin-walled I-section strut of length L made from a linear elastic, homogeneous and isotropic material with Young's modulus E and Poisson's ratio ν. Figure 2 shows the coordinate system and the cross-section properties where the web

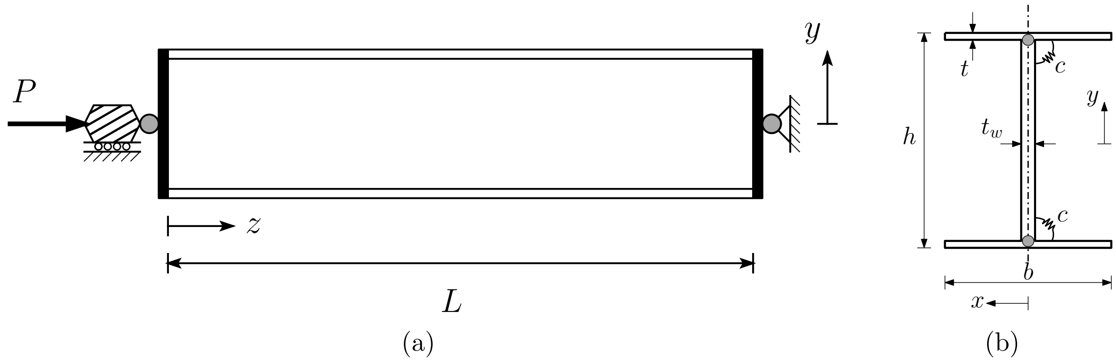

Figure 2: (a) Elevation of an I-section strut of length L that is compressed axially by a force P. The vertical and longitudinal coordinates are y and z respectively. (b) Strut cross-section with two equal flanges of width b and thickness t, and a web with height $(h - 2t)$ and thickness t_w. The transverse coordinate is x and the total cross-sectional area is A.

thickness $t_w = 2t$ since the I-section is assumed to be composed of two (C-shaped) channel members connected back-to-back; a type of arrangement that has been used in previous experimental studies [14, 6, 19] and assumed in previous analytical work [11, 12]. It was also demonstrated previously that local buckling in the web cannot occur before any local buckling in the flanges, since the web is twice as thick as the flanges and the height of the web is not sufficiently larger than the flange width. A recent and related study did consider the web deflecting in sympathy [20], but that case is practically confined to cross-sections with uniform thickness, which reduces the local buckling stress of the web significantly.

The relative fixity between the web and the flanges is represented by rotational springs with stiffness c that constrain the rotation at the flange–web joint about the z-axis, whereas the outstands remain free, as shown in Figure 2(b). Note that the two limiting cases, where the web is assumed to provide a pinned or a rigid support to the flanges, are associated with the conditions $c = 0$ and $c \to \infty$ respectively.

2.1. Modal descriptions

The local buckling mode profile of the flange plate in the transverse direction x is dependent on the rotational stiffness c. The local out-of-plane displacement $w_f(x, z)$ is defined as $f(x)w(z)$, where $f(x)$ represents the deflected shape in the transverse direction, as shown in Figure 3(a). A general form for $f(x)$ is derived from the limiting conditions

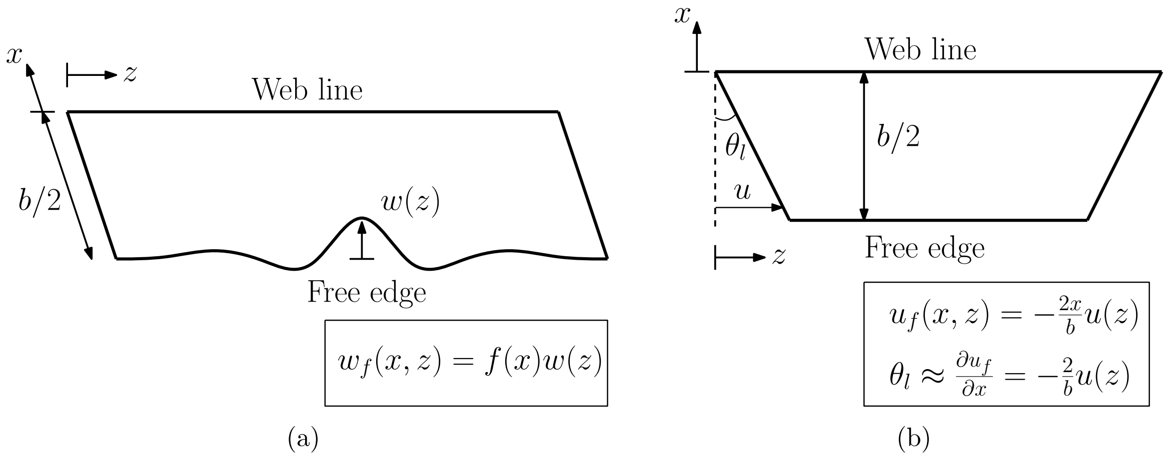

Figure 3: (a) Definition of the local out-of-plane displacement, $w_f(x, z)$, where $f(x)$ changes with increasing rotational stiffness c. (b) Definition of the local in-plane displacement $u_f(x, z)$, where a linear distribution is assumed across the width of the flange due to the assumption of Timoshenko beam bending of the flange in the xz plane.

of a beam and a cantilever strut such that the cases for pinned or rigid flange–web joint conditions may be described, thus:

$$f(x) = F_0 + F_1\left(\frac{2x}{b}\right) + F_2\left(\frac{2x}{b}\right)^2 + F_3\left(\frac{2x}{b}\right)^3 + F_4 \sin\frac{\pi x}{b}, \tag{1}$$

where F_0, F_1, F_2, F_3 and F_4 are the coefficients that are determined by the boundary conditions:

$$f(0) = 0, \quad Df''(0) = -cf'(0), \quad f''(-b/2) = 0, \quad f'''(-b/2) = 0, \tag{2}$$

with $D = Et^3/[12(1-\nu^2)]$ being the flange plate flexural rigidity, and primes refer to derivatives with respect to the transverse coordinate x. Substituting the corresponding expressions into the boundary conditions, F_0 and F_3 are found to be zero, whereas F_2 and F_4 can be expressed in terms of F_1 as s_2F_1 and s_4F_1 respectively, with s_2 and s_4 being determined as:

$$s_2 = \frac{\tilde{c}\pi}{4(\tilde{c}-\pi)}, \quad s_4 = \frac{2\tilde{c}}{\pi(\pi-\tilde{c})}, \tag{3}$$

and $\tilde{c} = cb/D$. The expression for F_1 is determined by a normalizing condition that fixes the amplitude to unity, $f(-b/2) = 1$. The full expression of the out-of-plane deflection $w_f(x, z)$ thus becomes:

$$w_f(x,z) = \frac{w(z)}{(s_2 - s_4 - 1)}\left[\frac{2x}{b} + s_2\left(\frac{2x}{b}\right)^2 + s_4 \sin\frac{\pi x}{b}\right]. \tag{4}$$

As stated earlier, the current study focuses on two limiting cases. First, the case of the pinned flange–web joint, as shown in Figure 4(a), can be deduced as $c \to 0$, hence $f(x) =$

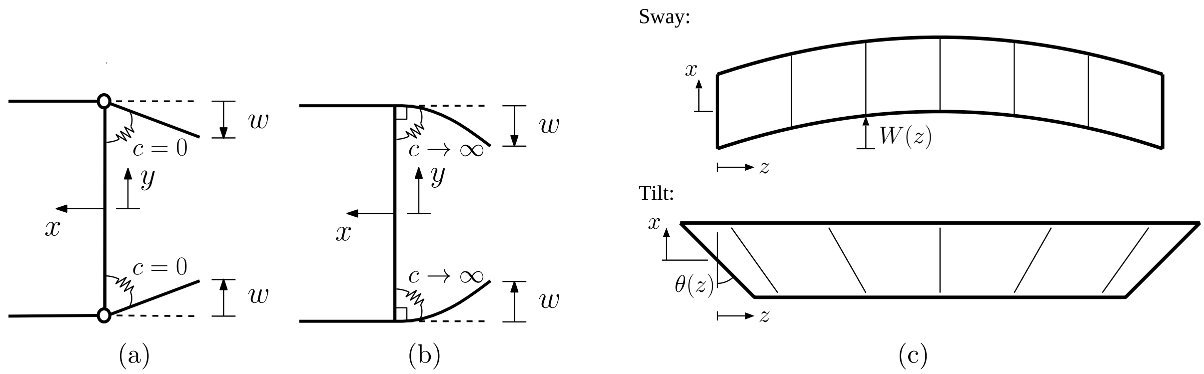

Figure 4: (a) and (b) show the out-of-plane flange displacement functions $w_f(x, z)$ of local buckling with amplitude w, when $c \to 0$ and $c \to \infty$ respectively; note that the web is assumed to be rigid; (c) shows the sway and tilt components of the global buckling mode about the cross-section weak axis of bending.

$-2x/b$. Second, the case of a rigid flange–web joint, as shown in Figure 4(b), can be deduced as $c \to \infty$ implying that $f(x)$ becomes:

$$f(x) = \left[\frac{4\pi}{8 + \pi^2 - 4\pi}\right] \left[\frac{2x}{b} + \frac{\pi}{4}\left(\frac{2x}{b}\right)^2 - \frac{2}{\pi}\sin\frac{\pi x}{b}\right]. \tag{5}$$

It is assumed that the local in-plane displacement function, $u_f(x, z)$ has a linear distribution across the flange width due to the assumption of Timoshenko bending, as shown in Figure 3(b), hence:

$$u_f(x, z) = -\frac{2x}{b}u(z). \tag{6}$$

The global buckling mode description also follows Timoshenko bending theory, introducing the shear strain which has been shown to be crucial in modelling local–global mode interaction [21]. Decomposing the global buckling mode into separate degrees-of-freedom known as 'sway' and 'tilt', the corresponding lateral displacement W and the rotation of the plane section θ are therefore:

$$W(z) = q_s L \sin\frac{\pi z}{L}, \quad \theta(z) = q_t \pi \cos\frac{\pi z}{L}, \tag{7}$$

as shown in Figure 4(c) with q_s and q_t being the generalized coordinates defining the respective amplitudes.

As presented previously [11], an additional set of local displacement functions, representing the less compressed portion of the flange needs to be introduced for the perfect strut where local buckling is critical. However, for the current model with the introduced rotational springs, it was found that an excessively fine discretization and numerous continuation attempts were required within the numerical continuation software Auto [17] to overcome significant convergence problems that often occurred after the bifurcation triggering global buckling. To reduce the computational expense without commensurately reducing model accuracy, a local imperfection is introduced to the more compressed half of the flange only, which imposes the break in symmetry from the beginning of each computation such that the global mode is introduced automatically. Therefore, an out-of-plane deflection $w_0(x, z)$ is introduced as the initial imperfection:

$$w_0(x, z) = f(x) A_0 \operatorname{sech}\left[\alpha\left(\frac{z}{L} - \eta\right)\right] \cos\left[\beta\pi\left(\frac{z}{L} - \eta\right)\right], \tag{8}$$

with $z = [0, L]$, A_0 being the amplitude and the imperfection is assumed to be symmetric about $z = \eta$. This expression is derived from a leading-order solution to a multiple scale perturbation analysis of a strut on a nonlinear softening foundation, which matches the least stable localized buckling mode shape closely [22]. The quantities α and β control the degree of localization and the periodic frequency of the imperfection shape respectively and are currently chosen to match the initial local buckling eigenmode found in earlier work [23].

2.2. Total potential energy and governing equations

The derivation of the total potential energy functional V follows a similar approach as found in [11] and [12]. The local imperfection is introduced by assuming the initial out-of-plane deflection w_0 is stress-relieved when the bending curvature $\chi = \chi_0$ [3, 24], implying that the elemental moment M and thus the local bending energy drops to zero, as illustrated in Figure 5. The global bending energy U_{bo} is given by the following expression:

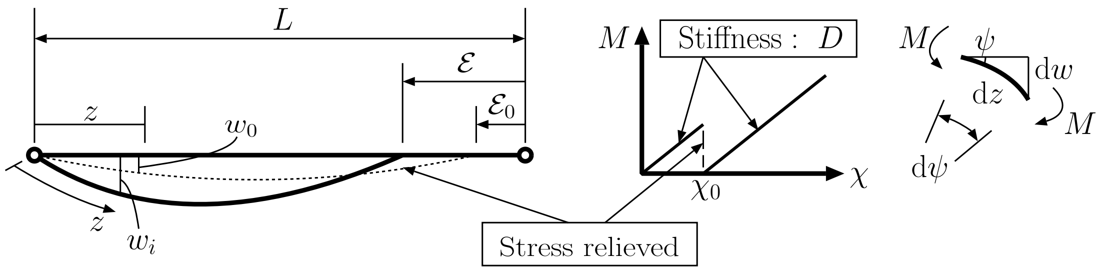

Figure 5: Introduction of a local geometric imperfection w_0 in the flange plates. The quantities $\mathcal{E}_0$ and $\mathcal{E}$ are the initial and final end-shortening respectively. The elemental bending moment is M, the initial and final bending curvatures are χ_0 and χ, and ψ is the local rotation angle from bending.

$$U_{bo} = \frac{1}{2} E I_w \int_0^L q_s^2 \frac{\pi^4}{L^2} \sin^2 \frac{\pi z}{L} \, \mathrm{d}z, \tag{9}$$

where I_w is the second moment of area of the web about the global weak axis. The local bending energy U_{bl} accounting for both top and bottom flanges is determined by the standard expression for the incremental strain energy from plate bending [25], including the contribution from the initial out-of-plane displacement w_0:

$$U_{bl} = D \int_{-b/2}^{0} \int_{0}^{L} \left[\left(\frac{\partial^2 w}{\partial z^2} - \frac{\partial^2 w_0}{\partial z^2} \right) + \left(\frac{\partial^2 w}{\partial x^2} - \frac{\partial^2 w_0}{\partial x^2} \right) \right]^2 - 2\left(1-\nu\right) \left[\left(\frac{\partial^2 w}{\partial z^2}\frac{\partial^2 w}{\partial x^2} - \frac{\partial^2 w_0}{\partial z^2}\frac{\partial^2 w_0}{\partial x^2} \right) - \left(\frac{\partial^2 w}{\partial z \partial x} - \frac{\partial^2 w_0}{\partial z \partial x} \right)^2 \right] \mathrm{d}z\,\mathrm{d}x. \tag{10}$$

The local bending energy U_{bl} accounting for both top and bottom flanges including the local imperfection is thus:

$$U_{bl} = D \int_0^L \Big[\{f^2\}_x \left(\ddot{w} - \ddot{w}_0\right)^2 + \{f''^2\}_x \left(w - w_0\right)^2 - 2\nu\{ff''\}_x \left(\ddot{w}w - \ddot{w}_0 w_0\right) + 2\left(1-\nu\right)\{f'^2\}_x \left(\dot{w} - \dot{w}_0\right)^2 \Big] \mathrm{d}z, \tag{11}$$

where dots represent derivatives with respect to z; the braces with subscript x denote that a definite integration has been performed with respect to x for the range from $-b/2$ to 0, for example:

$$\{Q\}_x \equiv \int_{-b/2}^{0} Q(x)\,\mathrm{d}x, \tag{12}$$

where Q is an example function. The integration is performed in the commercial computer algebra software MAPLE [26]; the fully integrated expressions are lengthy and are therefore not presented currently in explicit form for the sake of brevity.

The membrane strain energy U_m is derived by considering the longitudinal component of the direct strains ε_z and the shear strains γ_{xz} in the flanges. The general expressions for the direct strains, ε_{zt} and ε_{zc}, in the less and more compressed parts of the flange respectively are:

$$\begin{aligned} \varepsilon_{zt} &= \frac{\partial u_t}{\partial z} - \Delta, \\ \varepsilon_{zc} &= \frac{\partial u_t}{\partial z} - \Delta + \frac{\partial u_f}{\partial z} + \frac{1}{2}\left[\left(\frac{\partial w_f}{\partial z}\right)^2 - \left(\frac{\partial w_0}{\partial z}\right)^2 \right], \end{aligned} \tag{13}$$

where $u_t = -x\theta$, which is the in-plane displacement from the tilt component of the global buckling mode. A pure in-plane compressive strain Δ, which applies to the entire cross-section, is also included. The membrane energy from the direct strain U_d, accounting for the web with both top and bottom flanges including the local imperfection, is thus:

$$\begin{aligned} U_d = Etb \int_0^L \Big\{ & q_t^2 \frac{b^2\pi^4}{12L^2} \sin^2 \frac{\pi z}{L} + q_t \frac{b\pi^2}{6L} \sin \frac{\pi z}{L} \left[\frac{6\{xf^2\}_x}{b^2} \left(\dot{w}^2 - \dot{w}_0^2\right) - \dot{u} \right] \\ & + \frac{\{f^4\}_x}{4b} \left(\dot{w}^2 - \dot{w}_0^2\right)^2 + \frac{1}{6}\dot{u}^2 - \frac{2\{xf^2\}_x}{b^2} \dot{u} \left(\dot{w}^2 - \dot{w}_0^2\right) \\ & + \Delta \left[\left(1 + \frac{h}{b}\right)\Delta - \frac{1}{2}\dot{u} - \frac{\{f^2\}_x}{b} \left(\dot{w}^2 - \dot{w}_0^2\right) \right] \Big\} \mathrm{d}z. \end{aligned} \tag{14}$$

The presence of shear strain, the contributions of which are γ_{xzt} and γ_{xzc} in the less and more compressed parts of the flanges respectively, also adds to the membrane energy, the general expressions being:

$$\begin{aligned}\gamma_{xzt} &= \frac{\partial W}{\partial z} - \theta, \\ \gamma_{xzc} &= \frac{\partial W}{\partial z} - \theta + \frac{\partial u_f}{\partial x} + \frac{\partial w_f}{\partial z}\frac{\partial w_f}{\partial x} - \frac{\partial w_0}{\partial z}\frac{\partial w_0}{\partial x}.\end{aligned} \tag{15}$$

The membrane strain energy contribution from the shear strain U_s, accounting for both top and bottom flanges including the local imperfection, is thus:

$$\begin{aligned}U_s = Gtb \int_0^L \Bigg\{ &(q_s - q_t)^2 \pi^2 \cos^2 \frac{\pi z}{L} - \frac{2}{b} (q_s - q_t) \pi \cos \frac{\pi z}{L} \left[u - \{f'f\}_x (\dot{w}w - \dot{w}_0 w_0)\right] \\ &+ \frac{2}{b^2} \left[u^2 + \frac{b}{2}\{f'^2 f^2\}_x (\dot{w}w - \dot{w}_0 w_0)^2 - 2\{f'f\}_x u (\dot{w}w - \dot{w}_0 w_0)\right]\Bigg\} \, \mathrm{d}z,\end{aligned} \tag{16}$$

with $G = E/[2(1+\nu)]$ being the shear modulus. The strain energy stored in the rotational spring, U_{sp}, accounting for the top and bottom flanges, is given by the following expression:

$$U_{sp} = \int_0^L c \left[\frac{\partial}{\partial x} w_f(0, z)\right]^2 \mathrm{d}z \quad = \frac{c}{b^2} \int_0^L (2 + s_4 \pi)^2 w^2 \, \mathrm{d}z. \tag{17}$$

Finally, the work done by the axial load $P\mathcal{E}$ is given by:

$$P\mathcal{E} = P \int_0^L \left(\frac{1}{2} q_s^2 \pi^2 \cos^2 \frac{\pi z}{L} - \frac{1}{2}\dot{u} + \Delta\right) \mathrm{d}z, \tag{18}$$

where $\mathcal{E}$ is the end-displacement and comprises contributions due to global buckling, local buckling and from pure compression respectively. The total potential energy V is thus:

$$V = U_{bo} + U_{bl} + U_d + U_s + U_{sp} - P\mathcal{E}. \tag{19}$$

The governing differential equations are obtained by performing the calculus of variations on the total potential energy V following the well established procedure presented in the authors' previous work [11, 12]. The integrand of the total potential energy V can be expressed as a Lagrangian ($\mathcal{L}$) of the form:

$$V = \int_0^L \mathcal{L}(\ddot{w}, \dot{w}, w, \dot{u}, u, z) \, \mathrm{d}z, \tag{20}$$

with the first variation of V being given by:

$$\delta V = \int_0^L \left[\frac{\partial \mathcal{L}}{\partial \ddot{w}} \delta \ddot{w} + \frac{\partial \mathcal{L}}{\partial \dot{w}} \delta \dot{w} + \frac{\partial \mathcal{L}}{\partial w} \delta w + \frac{\partial \mathcal{L}}{\partial \dot{u}} \delta \dot{u} + \frac{\partial \mathcal{L}}{\partial u} \delta u\right] \mathrm{d}z. \tag{21}$$

To find the equilibrium states, V must be stationary, which requires the first variation δV to vanish for any small change in w and u. Since $\delta\ddot{w} = \mathrm{d}(\delta\dot{w})/\,\mathrm{d}z$, $\delta\dot{w} = \mathrm{d}(\delta w)/\,\mathrm{d}z$ and similarly $\delta\dot{u} = \mathrm{d}(\delta u)/\,\mathrm{d}z$, integration by parts allows the development of the Euler–Lagrange equations for w and u; these comprise a fourth order ordinary differential equation (ODE) for w and a second order ODE for u:

$$\begin{aligned} \frac{\mathrm{d}^2}{\mathrm{d}z^2}\left(\frac{\partial\mathcal{L}}{\partial\ddot{w}}\right) - \frac{\mathrm{d}}{\mathrm{d}z}\left(\frac{\partial\mathcal{L}}{\partial\dot{w}}\right) + \frac{\partial\mathcal{L}}{\partial w} &= 0, \\ \frac{\mathrm{d}}{\mathrm{d}z}\left(\frac{\partial\mathcal{L}}{\partial\dot{u}}\right) - \frac{\partial\mathcal{L}}{\partial u} &= 0. \end{aligned} \tag{22}$$

Stationary V also introduces three further equilibrium equations thus:

$$\frac{\partial V}{\partial q_s} = 0, \quad \frac{\partial V}{\partial q_t} = 0, \quad \frac{\partial V}{\partial \Delta} = 0. \tag{23}$$

The boundary conditions for w and u and their derivatives are for pinned end conditions for $z = 0$ and for symmetry at $z = L/2$:

$$w(0) = \ddot{w}(0) = \dot{w}(L/2) = \dddot{w}(L/2) = u(L/2) = 0, \tag{24}$$

with a further condition from matching the in-plane strain:

$$\frac{1}{3}\dot{u}(0) + \frac{2\{xf^2\}_x}{b^2}\dot{w}^2(0) - \frac{1}{2}\Delta + \frac{P}{2Etb} = 0, \tag{25}$$

noting that all of the boundary conditions can also be derived from the principle that V is stationary [21].

Linear eigenvalue analysis is conducted to determine the global buckling load P_o^{C}, which is identical for the pinned or rigid flange–web joints [11]. This is because the rotational spring stores no energy during global buckling and also $q_s = q_t = w = u = 0$ in fundamental equilibrium; the expression determined is thus:

$$P_o^{\mathrm{C}} = \frac{\pi^2 E I_w}{L^2} + \frac{2Gtb}{1 + 12GL^2/\left(E\pi^2 b^2\right)}. \tag{26}$$

Therefore, the average stress during global buckling is $\sigma_o^{\mathrm{C}} = P_o^{\mathrm{C}}/A$, whereas the local buckling load is given as $P_l^{\mathrm{C}} = A\sigma_l^{\mathrm{C}}$, where σ_l^{C} is the local buckling stress thus:

$$\sigma_l^{\mathrm{C}} = k_p \frac{D\pi^2}{t(b/2)^2} \tag{27}$$

and A is the total cross-section area. The coefficient k_p for a long rectangular plate is approximately 0.426 for one longitudinal edge simply supported and 1.25 for a rectangular plate with one longitudinal edge rigid, while the other longitudinal edge remains free in both cases [18].

3. Parametric study

Numerical computations are performed in the well-known continuation and bifurcation software AUTO [17]. A set of example equilibrium diagrams for cases where global or local buckling is critical is illustrated diagrammatically in Figures 6(a) and (b) respectively. Note that the perfect strut is analysed for cases where global buckling is critical, implying

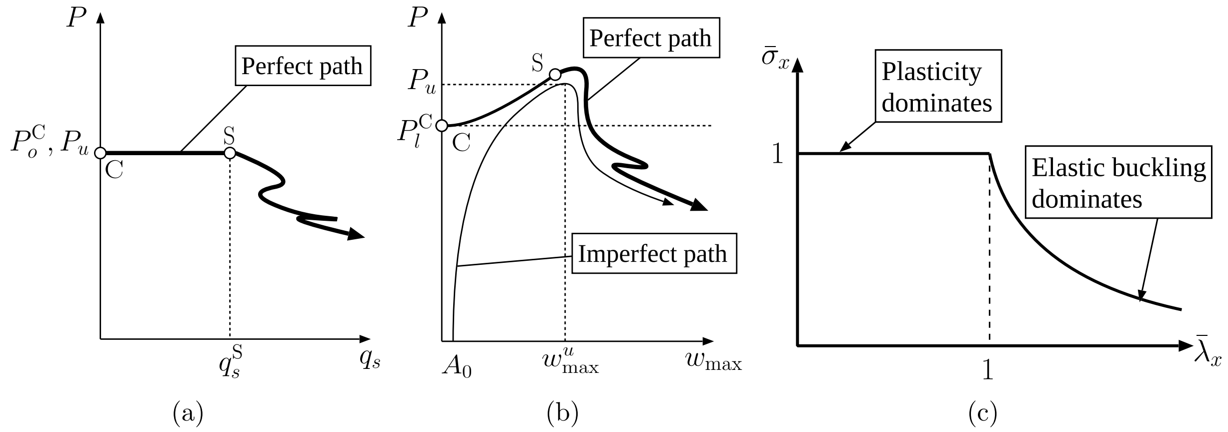

Figure 6: Sketches of equilibrium diagrams for (a) global buckling being critical where the perfect system is analysed and (b) local buckling being critical where a small local imperfection is introduced. (c) An idealized structural component strength curve in terms of normalized slenderness $\bar{\lambda}_x$ and stress $\bar{\sigma}_x$ – the subscripts shown as "x" may be changed to "o" or "l" to denote the cases for global or local buckling respectively.

that the ultimate load $P_u = P_o^{\mathrm{C}}$; hence the global buckling amplitude at the ultimate load $q_s^{\mathrm{u}} = q_s^{\mathrm{S}}$, in which q_s^{S} corresponds to the q_s value at the secondary bifurcation point, where interactive buckling is triggered. On the other hand, a very small local imperfection is introduced for cases where local buckling is critical. Since plates exhibit stable post-buckling paths, the ultimate load $P_u > P_l^{\mathrm{C}}$; the maximum out-of-plane deflection of the flange plates at the ultimate load is thus denoted as $w_{\max}^{\mathrm{u}}$. In all cases considered, the following properties are assumed – material: Young's modulus $E = 210$ kN/mm^2 and Poisson's ratio $\nu = 0.3$; geometry: flange thicknesses $t = 1.2$ mm, web thickness $t_w = 2t$ and the cross-section height $h = 120$ mm. The length L and the flange width b are both varied in the investigation.

3.1. Idealized strength relationships

It is well-known that the cause of failure is primarily due to structural instability in slender elements and plasticity in stocky elements. A measure of element slenderness has long since been established to classify the susceptibility to elastic instability or plastic collapse [27]. In the current case, the normalized global and local slendernesses $\bar{\lambda}_o$ and $\bar{\lambda}_l$ respectively can be defined where the subscript $x = \{o, l\}$:

$$\bar{\lambda}_x = \sqrt{\frac{f_{\mathrm{y}}}{\sigma_x^{\mathrm{C}}}}. \tag{28}$$

This is a positive non-dimensional quantity with f_{y} being the material yield stress, presently taken as 460 $\mathrm{N/mm^2}$, a standard value for cold-rolled structural steel [28]. The buckling stress, normalized with respect to f_{y}, where $\bar{\sigma}_x = \sigma_x^{\mathrm{C}}/f_{\mathrm{y}}$, defines the elastic buckling curve, thus:

$$\bar{\sigma}_x = (\bar{\lambda}_x)^{-2}. \tag{29}$$

The idealized buckling design curve is usually plotted in terms of the normalized stress and slenderness, as sketched in Figure 6(c). It is clear that when $\bar{\lambda}_x > 1$ the respective elements are relatively slender and elastic buckling dominates failure. However, for $\bar{\lambda}_x < 1$, the theoretical elastic buckling capacity of an element is higher than the material yield stress f_{y}, hence the element is in fact stocky and plasticity dominates with the failure stress being theoretically limited to f_{y}, if linear elasticity–perfect plasticity is assumed. With imperfections, however, the situation is less distinct and there is an imperfection sensitive region in the neighbourhood of $\bar{\lambda}_x = 1$ primarily due to the loss of elasticity during instability or a loss of stability after yielding. When $\bar{\lambda}_x \gg 1$, the ultimate load depends primarily on the purely elastic post-buckling characteristics with the effects of plasticity being of secondary importance. In the present study, the geometries are defined such that the $\bar{\lambda}_x$ values are clearly in the slender range.

3.2. Variation in strut length

The parametric investigation begins by varying the global slenderness $\bar{\lambda}_o$. The strut length L is principally changed while all other cross-section properties are kept constant. In this case, the flange width is taken to be a fixed value of $b = 96$ mm.

A critical strut length, denoted as L_c, is determined for the condition $P_o^{\mathrm{C}} = P_l^{\mathrm{C}}$. Numerical continuations are initially conducted with the strut length L being in the vicinity of L_c. It is obvious that, with such a condition, a secondary instability would be triggered almost simultaneously with the primary one. Increasing the strut length implies that the global buckling load P_o^{C} decreases; global buckling becomes critical and the secondary instability would be triggered at a larger value of q_s. With P_l^{C} being significantly larger than P_o^{C}, it would be expected that the flange plates would not buckle until a significant amount of global buckling deflection has developed. In those situations, phenomena such as plastic deformation may have been introduced before any interactive buckling. For the reasons of simplicity, a limiting mid-span deflection to length ratio q_s^{D} (taken presently as $1/500$) is taken as a "sufficiently large" limiting value for the global lateral deflection; hence cases where global buckling is critical and $q_s^{\mathrm{u}} > q_s^{\mathrm{D}}$ are considered to have effectively negligible mode interaction; the length where $q_s^{\mathrm{u}} = q_s^{\mathrm{D}}$ defines $L = L_o$. The interactive region where global buckling is critical is therefore defined for lengths $L_c < L < L_o$, which is illustrated diagrammatically in Figure 7(a). Note that the value of $L/500$, chosen arbitrarily in the current study, is used as an assumed imperfection size accounting for the manufacturing tolerances applied during the production of cold-rolled structural steel elements [29]; adjusting this value changes the range where interactive buckling is most significant. Of course, in reality, the aforementioned $L/500$ deflection, defined as q_s^{D}, would be in addition to any imposed initial global imperfection. This criterion is primarily one arising from concerns from serviceability requirements; for very slender struts, as are used exclusively in

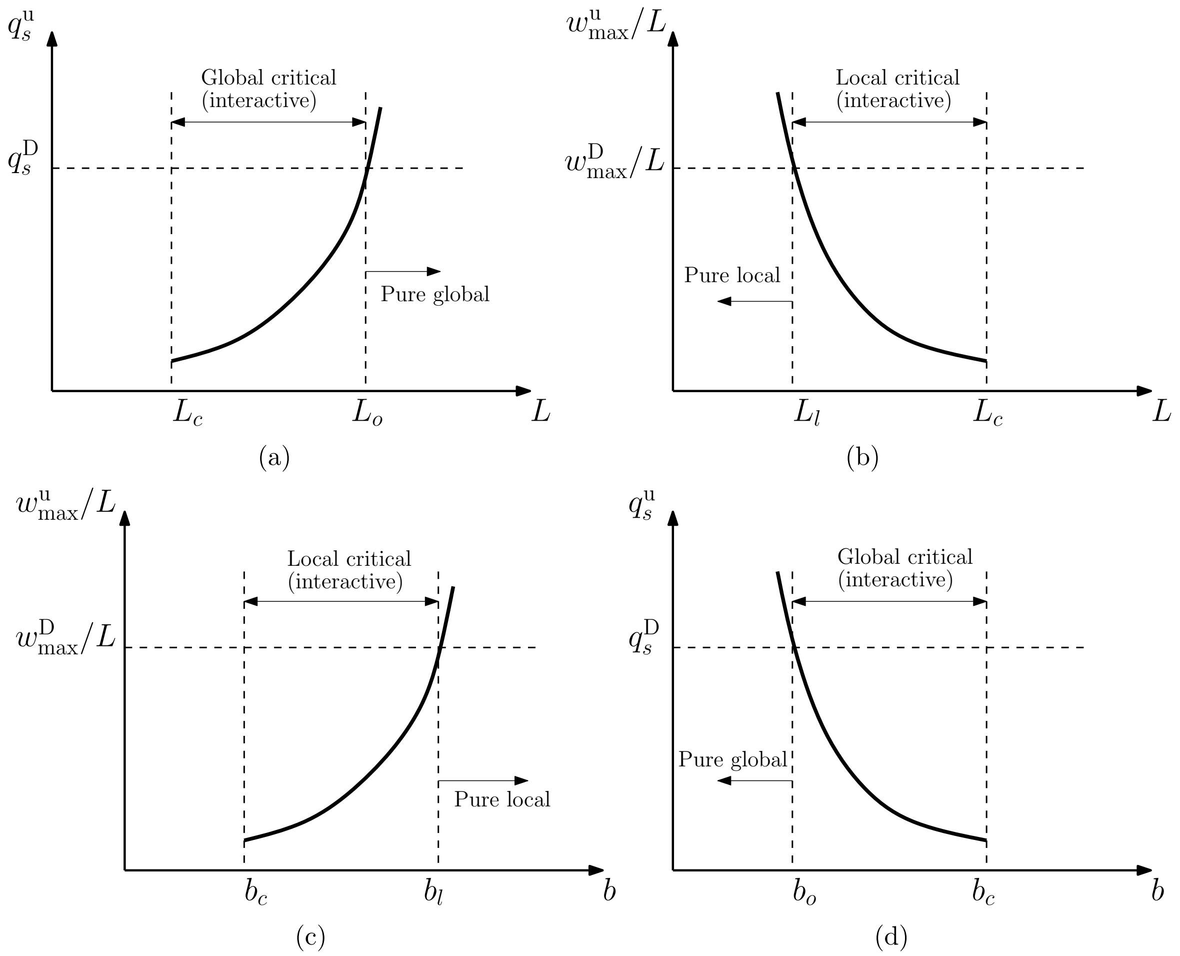

Figure 7: Interactive buckling regions while varying: (a–b) the strut length L and (c–d) the flange width b. The length $L = L_c$ and width $b = b_c$ are defined when $P_l^{\mathrm{C}} = P_o^{\mathrm{C}}$, whereas struts with $L > L_o$ (or $b < b_o$) and $L < L_l$ (or $b > b_l$) are assumed to exhibit pure global buckling and pure local buckling characteristics in the practical post-buckling range respectively.

the current study, an enormous amount of global deflection would need to occur if yielding were to be triggered.

Conversely, decreasing the strut length from L_c implies that local buckling becomes critical. Since the post-buckling characteristic of the pure local buckling of the flange plates is stable, the load rises with the increasing local deflection. It has been demonstrated in previous work [11] that the system exhibits an unstable interactive post-buckling path after the ultimate load P_u is reached. A similar concept is used for identifying the maximum local out-of-plane deflection $w^{\mathrm{u}}_{\mathrm{max}}$, which is illustrated diagrammatically in Figure 7(b). A limiting local flange deflection to length ratio, where $w^{\mathrm{u}}_{\mathrm{max}}/L = w^{\mathrm{D}}_{\mathrm{max}}/L$ defines the length $L = L_l$ where only pure local buckling occurs. Although the limit of $w^{\mathrm{D}}_{\mathrm{max}}/L$ is also set to $L/500$ currently, this again is chosen arbitrarily for serviceability concerns. However, strains in the flange may potentially become very large locally and ultimately violate a yield stress. Although it is possible to obtain the strains anywhere within the strut and it is therefore possible to measure when and where first yield occurs, this concern, however, is left for future work and elastic behaviour with a deflection criterion based on serviceability is implemented currently throughout. The interactive region where local buckling is critical therefore lies in the range: $L_l < L < L_c$. The same approach is applied to both cases where the flange–web joint is pinned or rigid.

3.3. Variation in flange width

A similar approach is applied to vary the local slenderness $\bar{\lambda}_l$, which depends primarily on the ratio b/t [27]. The flange width b is varied; the flange thickness t is as before and the strut length is fixed to $L = 2150$ mm.

For the given strut length, the critical flange width b_c is determined when $P^{\mathrm{C}}_o = P^{\mathrm{C}}_l$. Increasing b implies that P^{C}_l decreases whereas P^{C}_o increases, the latter due to the increase in the total weak-axis second moment of area; local buckling of the flange plates would therefore be critical. The same hypothesis, as for the cases where the strut length is varied, is applied and shown in Figure 7(c). It is considered that the strut with $b > b_l$ exhibits pure local buckling, whereas the interactive region where local buckling is critical is defined by $b_c < b < b_l$. Conversely, decreasing b below b_c implies that P^{C}_l increases whereas P^{C}_o decreases; global buckling would therefore be critical. Figure 7(d) shows the interactive region for b where global buckling is critical. Struts with a flange width smaller than b_o are considered to exhibit a purely global mode with insignificant modal interactions.

4. Numerical results and discussion

The parametric study is presented for each case where the flange–web joint is assumed to be pinned or rigid. For global buckling being critical ($P^{\mathrm{C}}_o < P^{\mathrm{C}}_l$), the perfect system is analysed implying that $w_0 = 0$, whereas for local buckling being critical ($P^{\mathrm{C}}_l < P^{\mathrm{C}}_o$), the equilibrium equations with small local imperfections are solved. The amplitude of the initial out-of-plane deflection A_0 is kept at a constant value of $t/100$ and the imperfection is assumed to be symmetric about midspan, hence $\eta = 1/2$. The value of A_0 is sufficiently small such that it may be considered to be a small perturbation to trigger the initial instability and the near-perfect system is analysed as far as possible. Numerical results are presented determining the ultimate strength of thin-walled I-section struts for a given range of lengths L as well as flange widths b. The normalized slendernesses are calculated using the expression in Equation (28), which all turn out to be clearly in the slender range for the examples studied – see Figure 6(c). It is worth recalling that the analytical model presented has been validated in earlier work [11, 12].

4.1. Pinned flange–web joint

Numerical continuations are initially conducted in AUTO for the strut with a pinned flange–web joint. The effect of varying the strut length L is first examined. It is observed in Figure 8 that for the flange width chosen, struts with lengths between $L_l = 2295$ mm

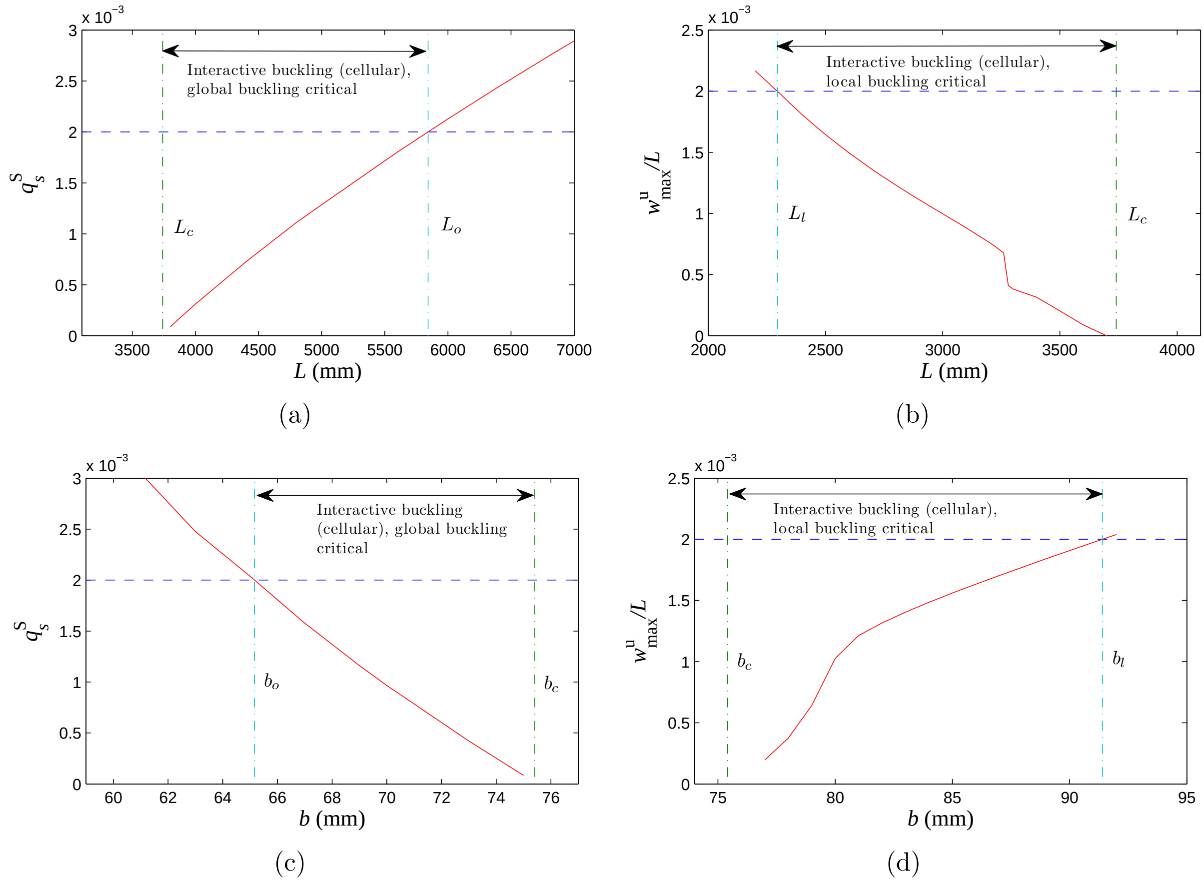

Figure 8: Results for the pinned flange–web case. (a–b) Strut length L and (c–d) flange width b varying. Normalized lateral displacement at the secondary bifurcation point $q_s^{\mathrm{S}}(= q_s^{\mathrm{u}})$ for (a) L varying and (c) b varying. Normalized maximum local out-of-plane displacement $w^{\mathrm{u}}_{\mathrm{max}}/L$ at the ultimate load P_u, versus (b) the strut length L and (d) the flange width b, for the cases where global buckling and local buckling are, respectively, critical. The vertical dot-dashed lines with labels L_c and b_c represent the critical strut length where $P_o^{\mathrm{C}} = P_l^{\mathrm{C}}$. The horizontal dashed line represents the amount of displacement above which interactive buckling is assumed to be insignificant; the interactive regions are therefore defined where $L_l < L < L_o$ and $b_o < b < b_l$, as shown by the vertical dot-dashed lines.

and $L_o = 5842$ mm are most vulnerable to interactive buckling, whereas struts with $L < L_l$ and $L > L_o$ are only practically vulnerable to pure local buckling and pure global buckling respectively. The critical strut length L_c, when $P_o^{\mathrm{C}} = P_l^{\mathrm{C}}$, is found to be approximately 3740 mm by both the theoretical expressions and the numerical solution. Figure 9(a) shows the load-carrying capacity P_u versus L. It is observed that for $L_c < L < L_o$, where

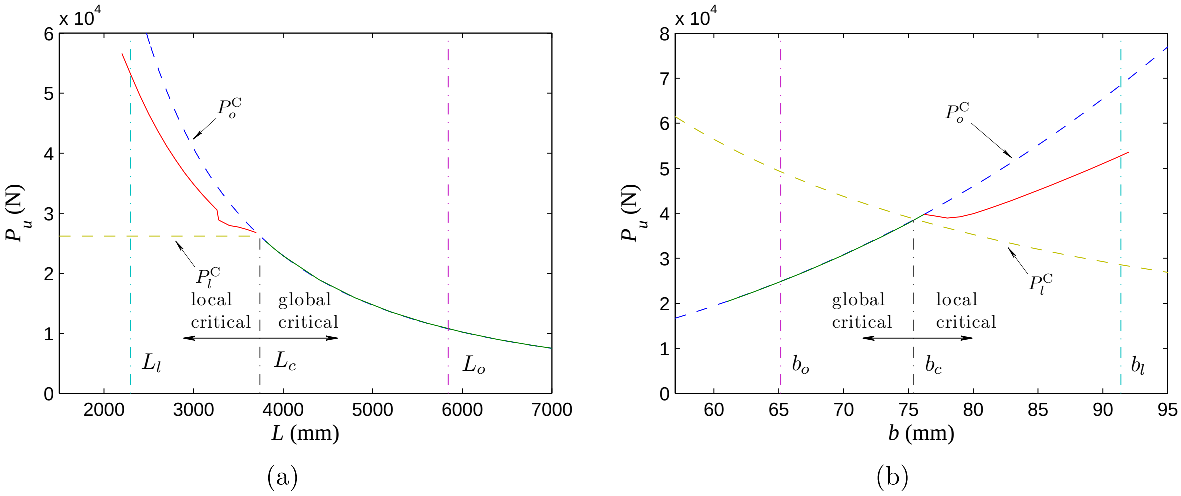

Figure 9: The ultimate load P_u versus (a) the strut length L and (b) the flange width b for the pinned flange–web case. The solid lines represent the actual numerical solutions whereas the dashed lines represent the theoretical calculations of the global and local buckling loads. Note that the local buckling load is independent of the strut length and is therefore represented by the horizontal dashed line in (a). The vertical dot-dashed lines represent lengths L_l, L_c and L_o directly corresponding to Figure 8.

global buckling is critical, $P_u = P_o^{\mathrm{C}}$ since global buckling is only weakly stable, whereas the interactive buckling behaviour, after the secondary instability (triggering the local buckling component) is encountered, is highly unstable. For strut lengths $L_l < L < L_c$, on the other hand, the load-carrying capacity P_u is capable of reaching a higher value than the local buckling load P_l^{C} due to the stable post-buckling behaviour of the flange plates. However, the load is not able to reach the global buckling load P_o^{C} due to the mode interaction after the secondary instability (this time triggering the global buckling component) is encountered.

Figure 9 is transformed, in a similar way to [15], into the central graph of Figure 10, which shows the normalized ultimate load P_u/P_l^{C} versus the ratio of the modal buckling loads $P_o^{\mathrm{C}}/P_l^{\mathrm{C}}$ for varying L. The graphs surrounding the main one show examples of the actual equilibrium paths, where the normalized load $p = P/P_o^{\mathrm{C}}$ is plotted against either the normalized global or local buckling amplitude. These graphs are shown for different strut lengths corresponding to different parts of the central graph, indicated by the arrows. It is observed that for $L > L_o$, the strut exhibits pure global buckling that is weakly (approximately neutrally) stable after the critical bifurcation point. For $L_c < L < L_o$, the strut exhibits a weakly stable equilibrium path after the critical bifurcation point, followed by an unstable interactive post-buckling path after the secondary bifurcation point. For

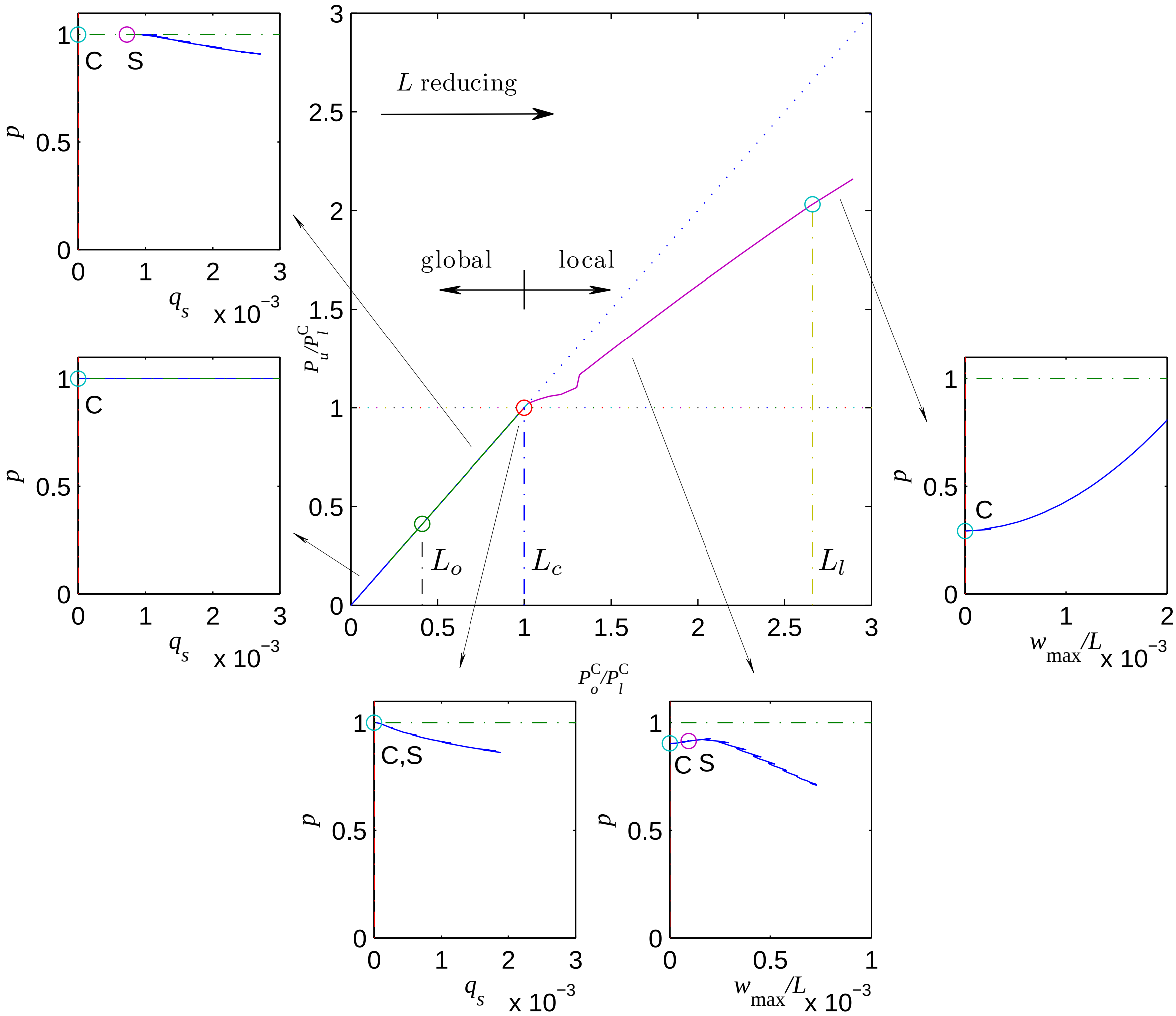

Figure 10: Generalized results for the pinned flange–web case with the strut length L varying. The central graph shows the normalized ultimate load P_u/P_l^{C} versus the ratio between the modal buckling loads $P_o^{\mathrm{C}}/P_l^{\mathrm{C}}$. The solid line represents the actual numerical solutions whereas the dot-dashed lines representing strut lengths L_l, L_c and L_o correspond directly to Figure 9(a). The surrounding graphs show examples of the equilibrium paths, where the normalized load $p = P/P_o^{\mathrm{C}}$, corresponding to different parts of the central graph, separated by the dot-dashed lines. Labels C and S correspond to the critical and the secondary bifurcation points. The surrounding graphs anti-clockwise from top-left respectively show cases for: $L = [L_c, L_o]$; $L > L_o$; $L = L_c$; $L = [L_l, L_c]$ and $L < L_l$.

$L \approx L_c$, the global and the local buckling modes are triggered practically simultaneously and the strut immediately exhibits a highly unstable interactive post-buckling path. For $L_l < L < L_c$, the strut exhibits a stable post-buckling path after the critical bifurcation, followed by an unstable interactive post-buckling path after the secondary bifurcation. Finally, for $L < L_l$, the strut exhibits pure local buckling of the flange plates that is strongly stable. Note that for $L_l < L < L_o$, all interactive post-buckling equilibrium paths exhibit the sequential snap-backs signifying cellular buckling behaviour [11, 7, 6].

The cross-section properties given in §3.3 and L are subsequently fixed and numerical continuations are conducted for the varying flange width b with Figures 8(c–d), 9(b) and 11 corresponding to Figures 8(a–b), 9(a) and 10 respectively. It is observed in Figure 8(c–d) that flanges with widths ranging between $b_o = 65$ mm and $b_l = 91$ mm are most vulnerable to interactive buckling behaviour, whereas flanges with $b > b_l$ and $b < b_o$ are only vulnerable to pure local buckling and pure global buckling respectively. The critical flange width b_c, when $P_o^C = P_l^C$, is found to be approximately 75 mm by both the theoretical expressions and the numerical solution. Figure 9(b) shows the load-carrying capacity P_u versus b. For global buckling being critical, or local buckling being critical, the post-buckling behaviour corresponds to the length variation case except that previously where lengths L were being increased, the flange widths b are decreased. Figure 11 shows a plot of P_u/P_l^C versus P_o^C/P_l^C for varying b and examples of the actual equilibrium paths for different ranges of b are shown with features very similar to Figure 10. It is worth re-emphasizing that all equilibrium paths exhibit cellular buckling behaviour within the interactive region defined as: $b_o < b < b_l$.

4.2. Rigid flange–web joint

Numerical continuations are now presented for struts with rigid flange–web joints. The strut length L is first varied with the cross-section properties given in §3.2. Figures 12, 13 and 14 correspond to Figures 8, 9 and 10, for the rigid flange–web joint, respectively. It is observed in Figure 12 that struts with lengths between $L_l = 1610$ mm and $L_o = 2680$ mm are most vulnerable to interactive buckling. The critical strut length L_c, when $P_o^C = P_l^C$, is found to be approximately 2185 mm by both the theoretical expressions and the numerical solution. Figure 13(a) shows a very similar trend as in Figure 9(a). However, one distinctive feature is that for 1800 mm $< L <$ 2300 mm, the ultimate load P_u is very close to the local buckling load P_l^C, whereas P_u only begins to be significantly higher than P_l^C for $L < 1800$ mm. This feature is also indicated by the sudden change in the slope of the curve in Figure 12(b). This is caused by the qualitatively different post-buckling behaviour after the secondary instability is triggered as observed in Figure 14; such a region was termed in [15] as the 'imperfection sensitive' zone. The point where P_u begins to deviate from P_l^C is denoted as L_s, as shown in Figures 12(b) and 13. The reduction in P_u caused by the nominal imperfection is approximately 10% when $L \approx L_c$. Figure 14 shows similar graphs as in Figure 10. However, it can be observed in Figure 14 that for $L_s < L < L_c$, the strut exhibits a strongly unstable interactive post-buckling path with a single snap-back, whereas for $L_l < L < L_s$, the strut exhibits an approximately neutral interactive post-buckling path, but after the secondary instability is triggered.

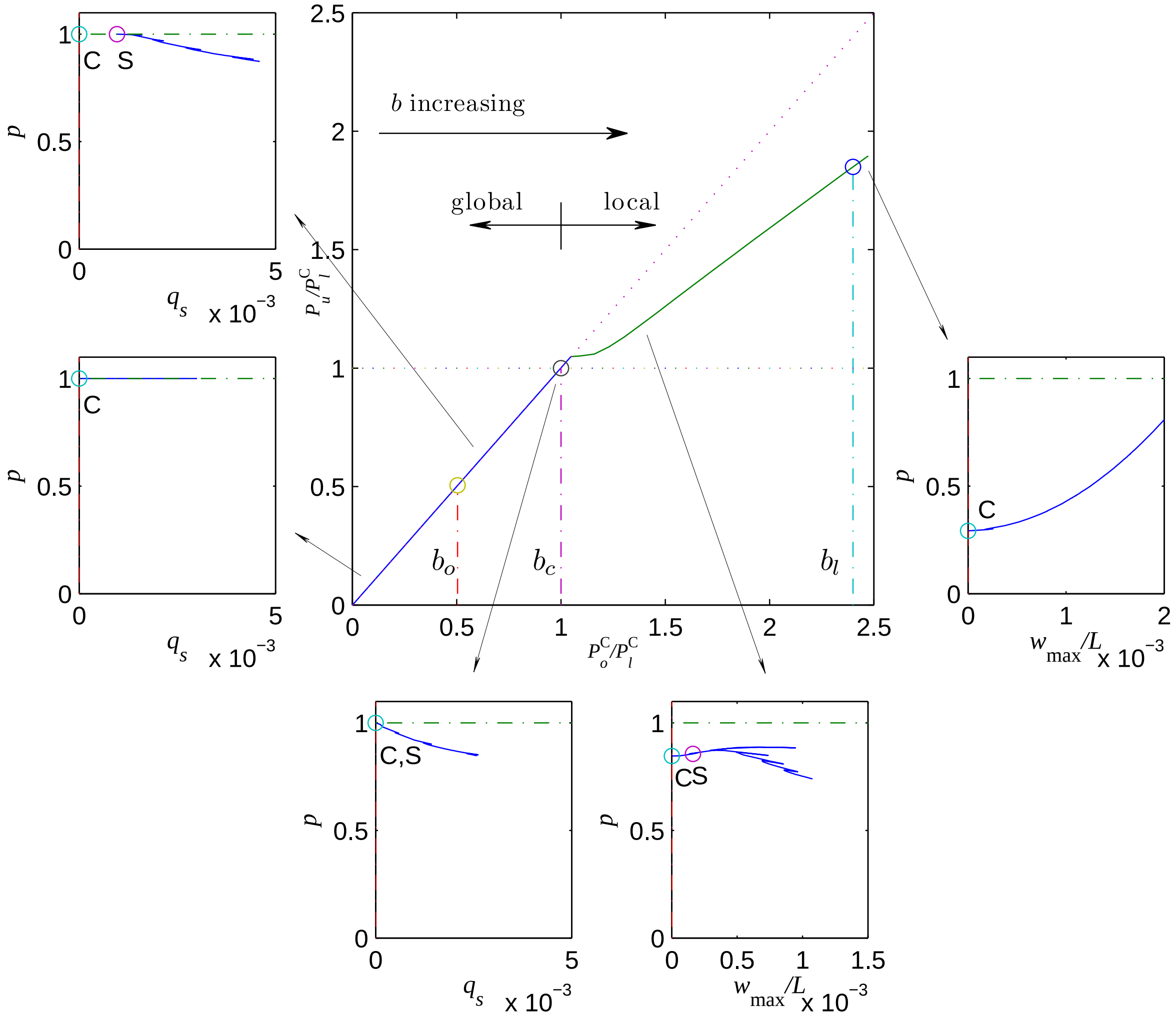

Figure 11: Generalized results for the pinned flange–web case with the flange width b varying. The central graph shows the normalized ultimate load P_u/P_l^{C} versus the ratio between the modal buckling loads $P_o^{\mathrm{C}}/P_l^{\mathrm{C}}$. The solid line represents the actual numerical solutions whereas the dot-dashed lines representing flange widths b_l, b_c and b_o correspond directly to Figure 9(b). The surrounding graphs show examples of the equilibrium paths corresponding to different parts of the central graph, separated by the dot-dashed lines. Labels C and S correspond to the critical and the secondary bifurcation points. The surrounding graphs anti-clockwise from top-left respectively show cases for: $b = [b_o, b_c]$; $b < b_o$; $b = b_c$; $b = [b_c, b_l]$ and $b > b_l$.

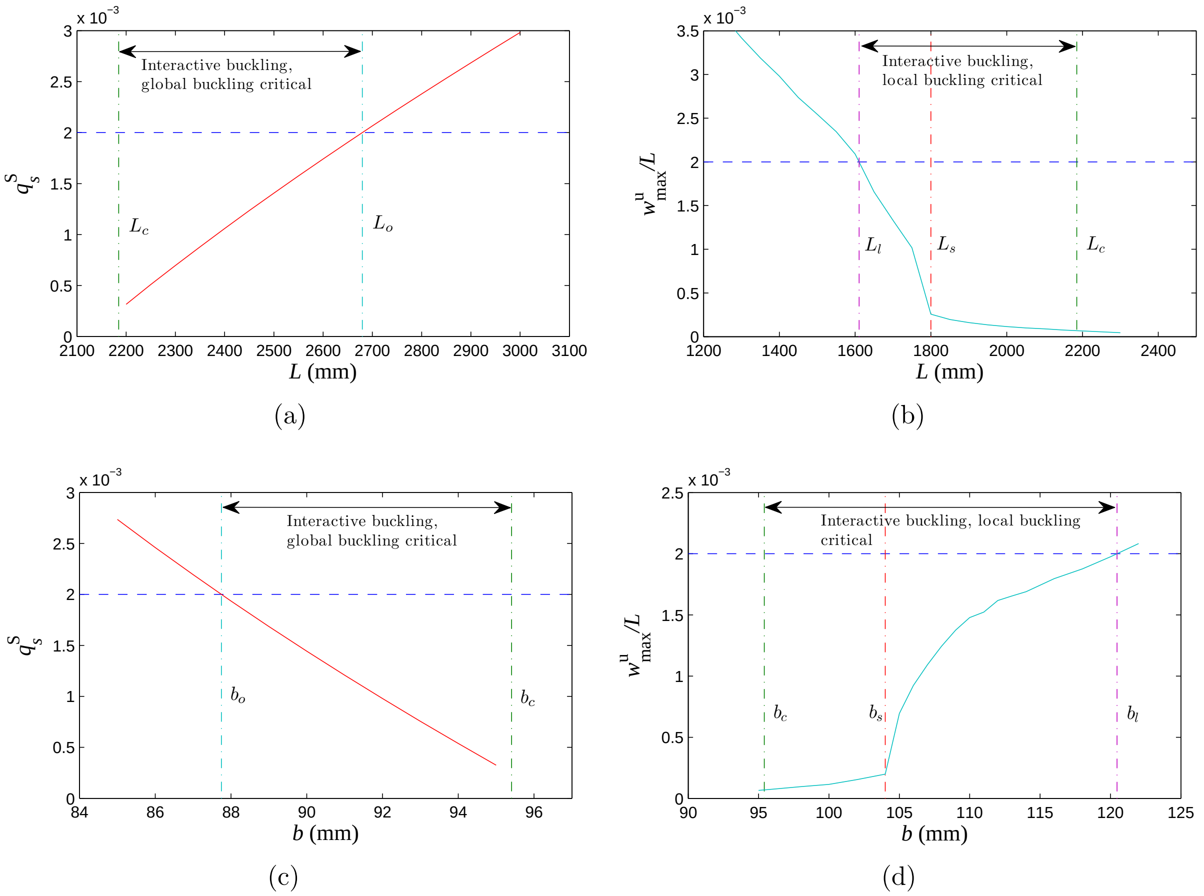

Figure 12: Results for the rigid flange–web case with (a–b) strut length L and (c–d) flange width b varying. Features are identical to Figure 8 but note the vertical dot-dashed lines L_s and b_s representing the strut length and the flange width respectively from which the secondary instability triggering global buckling occurs at significant values of local buckling displacement.

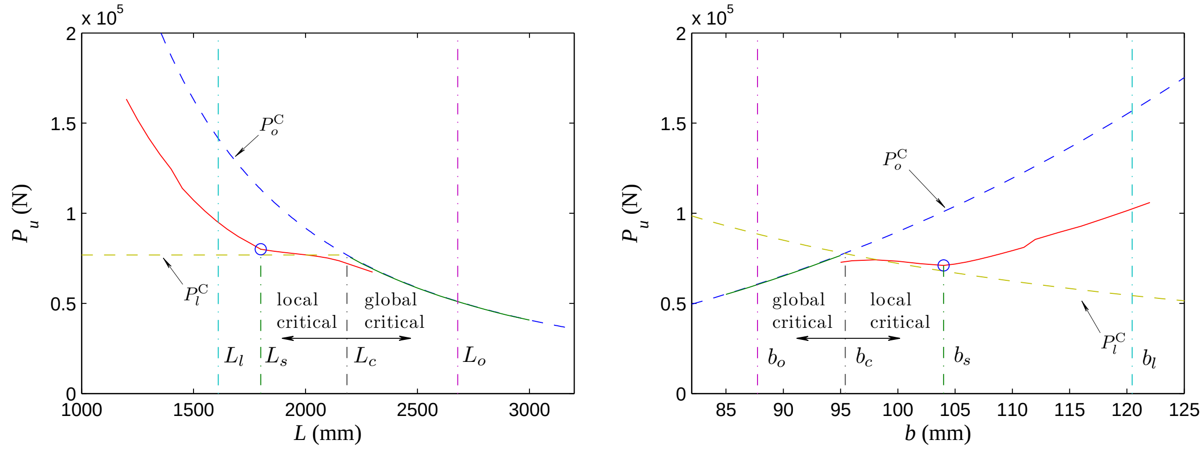

(a) (b)

Figure 13: The ultimate load P_u versus the (a) strut length L and (b) the flange width b for the rigid flange–web case. Features are identical to Figure 9 but note the vertical dot-dashed lines L_s and b_s representing the strut length and the flange width respectively from which P_u begins to deviate from P_l^{C} significantly.

The flange width b is also varied for the strut with a rigid flange–web joint, the geometric properties defined in §3.3 and the length L being fixed. It is observed in Figure 12(c–d) that struts with flange widths between $b_o = 88$ mm and $b_l = 120$ mm are most vulnerable to the interactive buckling behaviour. The flange width b_c when $P_o^{\mathrm{C}} = P_l^{\mathrm{C}}$ is found to be approximately 95 mm by both the theoretical expressions and the numerical solution. Figures 13(b) and 15 show a very similar trend as in Figures 9(b) and 11 respectively, but without the sequence of snap-backs that signify cellular buckling. Although no sequence of snap-backs was observed in the equilibrium paths, the post-buckling solutions still exhibited a characteristic change in local buckling wavelength in the flange plates [12]. This implies that the fundamental effect of the varying stress along the length induced by local–global mode interaction still affects the post-buckling mode even though no snap-backs are present in the equilibrium path [30]. Similar to the case where L is varied, it is observed that there is a clear transition in the post-buckling behaviour as b is increased from $b_o \to b_c \to b_s \to b_l$ and beyond, as shown in Figure 15.

Unlike the case of the pinned flange–web joint, with the strut length L_s or flange width b_s being pinpointed numerically, the central graphs in Figures 14 and 15 may be compared directly to Figure 1. With L_s and b_s defining the points where the post-buckling becomes neutral, albeit with the numerics including a small perturbation, the value of $1/\Psi$ (see Figure 1 where Ψ is the stiffness reduction factor) for the perfect case may be estimated by drawing a line from the origin of the main graph in either Figure 14 or Figure 15 to the point on the curve marked as L_l or b_l respectively and noting where the line crosses where $P_u/P_l^{\mathrm{C}} = 1$. It is determined that $1/\Psi \approx 1.6$ in both cases and so $\Psi \approx 0.63$ and the position marked as a circle in Figure 1 given by the expression $(1 + \Psi)/(2\Psi) \approx 1.25$ which corresponds to both main graphs in Figures 14 and 15 and are perfectly in accord with van

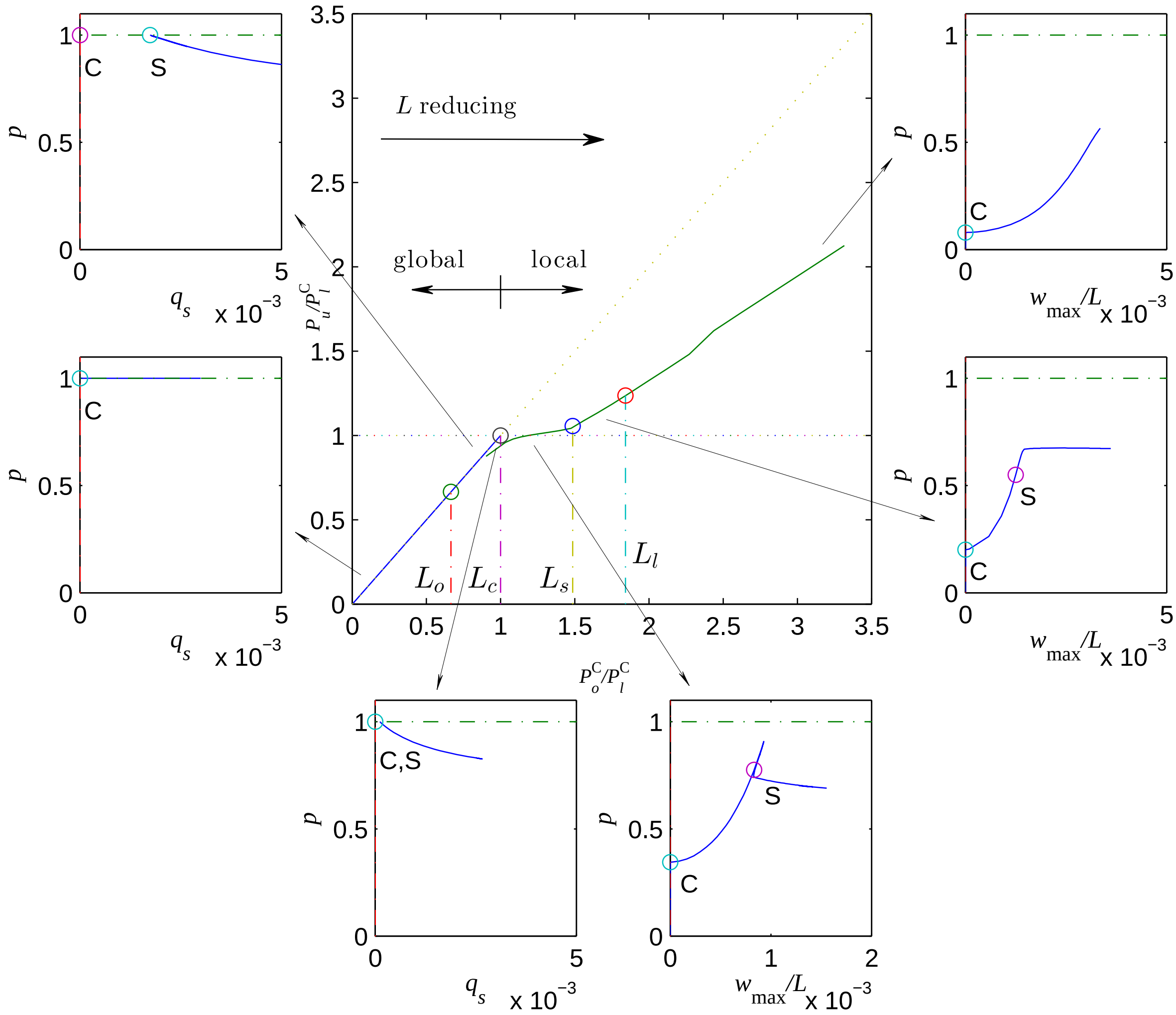

Figure 14: Generalized results for the rigid flange–web case with L varying. Features essentially identical to Figure 10 except that the surrounding graphs shown anti-clockwise from top-left are for the cases: $L = [L_c, L_o]$; $L > L_o$; $L = L_c$; $L = [L_s, L_c]$; $L = [L_l, L_s]$ and $L < L_l$.

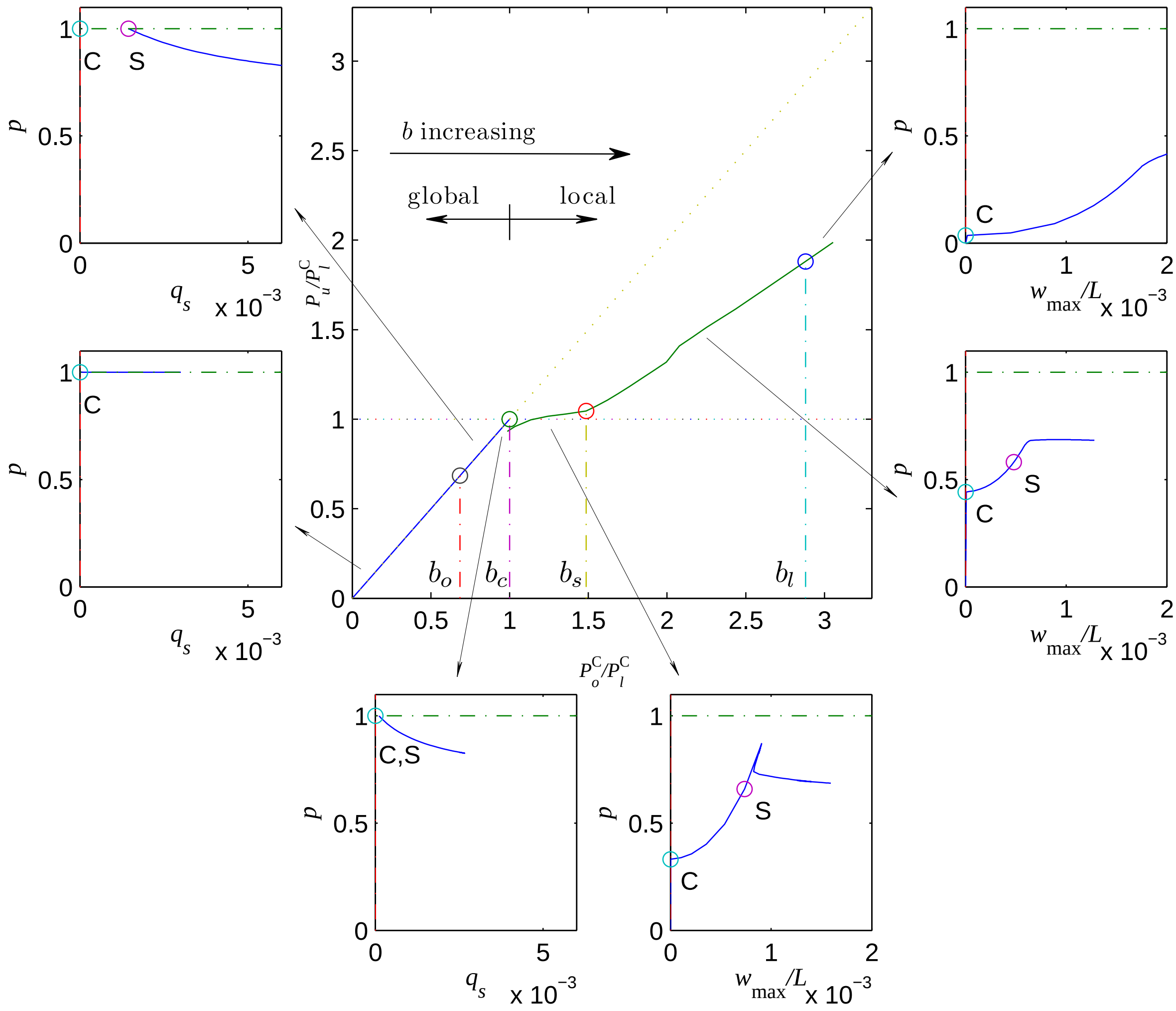

Figure 15: Generalized results for the rigid flange–web case with b varying. Features basically identical to Figure 11 except that the surrounding graphs shown anti-clockwise from top-left are for the cases: $b = [b_o, b_c]$; $b < b_o$; $b = b_c$; $b = [b_c, b_s]$; $b = [b_s, b_l]$ and $b > b_l$.

der Neut's general findings. The informed reader may notice that the stiffness reduction factor Ψ is quite high compared to [15], where Ψ was reported to be approximately 0.41. However, it should be noted that [15] effectively considers global buckling about the strong axis that induces local buckling in one flange, whereas the current model is focused on global buckling about the weak axis with two flange outstands buckling locally with rigid flange–web joints. Moreover, the analytical model has been validated previously using a shell finite element model [12] developed in the commercial code ABAQUS [31].

As a final remark, it is worth noting that there is no technical reason for corresponding quantities L_s and b_s not to be found for the pinned flange–web joint case. However, the precise locations of these quantities were difficult to pinpoint numerically owing to the many snap-backs present in the post-buckling response.

4.3. Interactive buckling zones

Tables 1 and 2 summarize, for both the pinned and the rigid flange–web joints, the

Joint-type	$\min(L_l, L_s)$ (mm)	$\bar{\lambda}_l$	L_c (mm)	$\bar{\lambda}_c$	L_o (mm)	$\bar{\lambda}_o$
Pinned	2300	3.00	3700	3.00	5800	4.68
Rigid	1800	1.76	2300	1.76	2700	2.17

Table 1: Summary of values for L_l, L_s, L_c and L_o, with $\bar{\lambda}_l$, $\bar{\lambda}_c$ and $\bar{\lambda}_o$ for struts with the properties given in §3.2, for both the pinned and the rigid flange–web joint cases.

Joint-type	$\min(b_l, b_s)$ (mm)	$\bar{\lambda}_l$	b_c (mm)	$\bar{\lambda}_c$	b_o (mm)	$\bar{\lambda}_o$
Pinned	92	2.88	74	2.31	65	2.88
Rigid	104	1.91	95	1.74	88	1.94

Table 2: Summary of values for b_l, b_s, b_c and b_o, with $\bar{\lambda}_l$, $\bar{\lambda}_c$ and $\bar{\lambda}_o$ for struts with the properties given in §3.3, for both the pinned and the rigid flange–web joint cases.

region where interactive buckling is significant and the post-buckling behaviour is highly unstable after the secondary instability is triggered, in terms of the strut length L and the flange width b respectively. It is clear that by increasing the rigidity of the flange–web joint, the vulnerability to unstable interactive buckling is reduced, in terms of the range of values for both the strut length L and the flange width b. The values of the global and the local normalized slendernesses, $\bar{\lambda}_o$ and $\bar{\lambda}_l$ respectively, are calculated using the expression in Equation (28). Note that the global and the local normalized slendernesses, for each critical strut length L_c and flange width b_c, are approximately equal, and therefore denoted as a single notation $\bar{\lambda}_c$. Also note that when L is varied, the local normalized slenderness remains unchanged, and therefore $\bar{\lambda}_c = \bar{\lambda}_l$. When b is varied, however, both global and local slendernesses change. The values of the global and local normalized slendernesses are plotted on the idealized strength curves in Figure 16.

It is of course worth recalling that a yield stress of 460 $\mathrm{N/mm^2}$ is assumed in the current study and that altering this value would numerically change the normalized slendernesses.

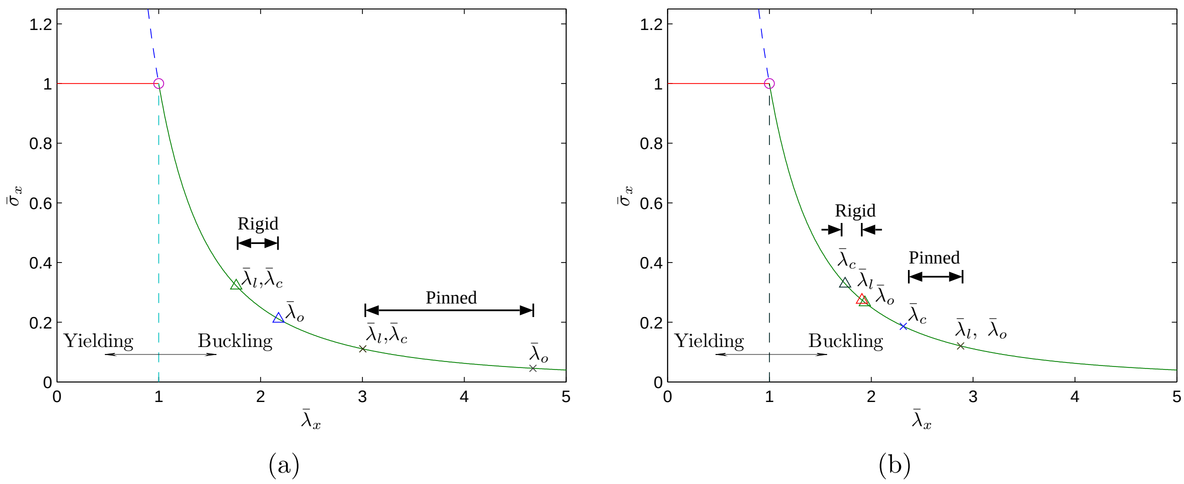

Figure 16: The idealized strength curves with the symbols representing the global and the local normalized slendernesses found in the parametric study for variations in (a) the strut length L and (b) the flange width b. Cross and triangular symbols represent the cases where the flange–web joint is assumed to be pinned and rigid respectively. For each joint-type, the range of slendernesses which defines the interactive buckling zone is shown.

It is observed that for the chosen set of cross-section properties, elastic buckling dominates the failure mechanism in the interactive region for all cases. The struts with rigid flange–web joints are less slender than those with pinned flange–web joints, and are therefore closer to the region where plasticity would begin to alter the behaviour significantly. Moreover, the range of slendernesses defining the interactive buckling zone is more confined when the flange–web joint is rigid. Nevertheless, for the chosen set of cross-section properties, it is justified that plasticity effects would be negligible. If a wider range of cross-section properties were to be considered, the presented procedure could be applied to investigate the possibility of any potential plasticity influence, *i.e.* $\bar{\lambda} \approx 1$, such that a better estimation for the true load-carrying capacity may be obtained.

These findings have practical consequences in that it is identified that there are parametric ranges that is sensitive to imperfections (for the rigid flange–web joint case: $L_s < L < L_c$ or $b_c < b < b_s$) and those that are primarily insensitive while the material remains elastic ($L > L_o$ and $L < L_s$ or $b < b_o$ and $b > b_s$). In terms of maximizing the load-carrying capacity, it seems that that strut lengths greater than L_o and flange widths less than b_o may be excessively large and small respectively for optimization purposes. However, in the ranges for the strut lengths $L_l < L < L_s$ and the flange widths $b_s < b < b_l$, these may be used for determining actual optimum geometries with relatively favourable nonlinear post-buckling behaviour. However, an optimization study could only be performed after a full imperfection-sensitivity study of all the parametric ranges is conducted with different material strengths considered – this is left for future work.

5. Concluding remarks

Parametric studies were conducted for an example set of thin-walled I-section strut geometries with two limiting cases where the web was assumed to provide a pinned or a rigid support to the flanges. The investigation focused on changing the global and the local slendernesses by varying the strut length and the flange width respectively. A simple deflection based criterion was defined such that an interactive buckling dominated region, where the interaction between the weak-axis global (Euler) buckling and the local flange plate buckling, may be determined.

For pinned flange–web joints, all struts within the interactive region exhibited unstable cellular buckling, including cases where either global or local buckling were critical. For rigid flange–web joints, struts for the cases where global buckling was critical, exhibited unstable post-buckling responses without the observation of cellular buckling response in the strict sense, *i.e.* without a sequence of snap-back instabilities, even though the post-buckling profiles still exhibited changing wavelengths [12]. However, for the cases where local buckling was critical, it was found that struts may exhibit two distinct post-buckling responses: a stable equilibrium path followed by a weakly unstable (approximately neutral) equilibrium path; or a stable equilibrium path followed by a highly unstable equilibrium path with a snap-back. It is the highly unstable post-buckling responses that should be avoided in design practice owing to the severe imperfection sensitivity associated with that characteristic response. It was also found that by increasing the rigidity of the flange–web joint, the potentially dangerous region within the elastic range became smaller.

The current methodology may be applied to determine the region where mode interaction dominates for a given set of basic geometries and materials, so long as the buckling occurs strictly within the elastic range. However, since the normalized slenderness for local and global buckling properties may be calculated, as can the strain levels within the strut throughout the loading history, the analysis can indicate clearly whether the strain levels exceed a yielding criterion before the ultimate load is reached. In those cases, plasticity effects [16] would need to be considered in a more sophisticated structural model.

References

[1] J. M. T. Thompson, G. W. Hunt, A general theory of elastic stability, Wiley, London, 1973.

[2] B. Budiansky (Ed.), Buckling of structures, Springer, Berlin, 1976.

[3] J. M. T. Thompson, G. W. Hunt, Elastic instability phenomena, Wiley, London, 1984.

[4] V. Gioncu, General theory of coupled instabilities, Thin-Walled Struct. 19 (2–4) (1994) 81–127. doi:10.1016/0263-8231(94)90024-8.

[5] M. Pignataro, M. Pasca, P. Franchin, Post-buckling analysis of corrugated panels in the presence of multiple interacting modes, Thin-Walled Struct. 36 (1) (2000) 47–66. doi:10.1016/S0263-8231(99)00027-0.

[6] M. A. Wadee, L. Gardner, Cellular buckling from mode interaction in I-beams under uniform bending, Proc. R. Soc. A 468 (2012) 245–268. doi:10.1098/rspa.2011.0400.

[7] M. A. Wadee, M. Farsi, Cellular buckling in stiffened plates, Proc. R. Soc. A 470 (2168) (2014) 20140094. doi:10.1098/rspa.2014.0094.

[8] D. Dubina, V. Ungureanu, Instability mode interaction: From Van Der Neut model to ECBL approach, Thin-Walled Structures 81 (2014) 39–49. doi:10.1016/j.tws.2013.10.014.

[9] M. Nassirnia, A. Heidarpour, X.-L. Zhao, J. Minkkinen, Innovative hollow corrugated columns: A fundamental study, Eng. Struct. 94 (2015) 43–53. doi:10.1016/j.engstruct.2015.03.028.

[10] M. A. Wadee, M. Farsi, Imperfection sensitivity and geometric effects in stiffened plates susceptible to cellular buckling, Structures 3 (2015) 172–186. doi:10.1016/j.istruc.2015.04.004.

[11] M. A. Wadee, L. Bai, Cellular buckling in I-section struts, Thin-Walled Struct 81 (2014) 89–100. doi:10.1016/j.tws.2013.08.009.

[12] L. Bai, M. A. Wadee, Mode interaction in thin-walled I-section struts with semi-rigid flange-web joints, Int. J. Non-Linear Mech. 69 (2015) 71–83. doi:10.1016/j.ijnonlinmec.2014.11.023.

[13] G. W. Hunt, M. A. Peletier, A. R. Champneys, P. D. Woods, M. A. Wadee, C. J. Budd, G. J. Lord, Cellular buckling in long structures, Nonlinear Dyn. 21 (1) (2000) 3–29. doi:10.1023/A:1008398006403.

[14] J. Becque, K. J. R. Rasmussen, Experimental investigation of the interaction of local and overall buckling of stainless steel I-columns, ASCE J. Struct. Eng. 135 (11) (2009) 1340–1348. doi:10.1061/(ASCE)ST.1943-541X.0000051.

[15] A. van der Neut, The interaction of local buckling and column failure of thin-walled compression members, in: M. Hetényi, W. G. Vincenti (Eds.), Proceedings of the 12th International Congress on Applied Mechanics, Springer, Berlin, 1969, pp. 389–399.

[16] J. Becque, Local–overall interaction buckling of inelastic columns: A numerical study of the inelastic Van der Neut column, Thin-Walled Struct. 81 (2014) 101–107. doi:10.1016/j.tws.2013.07.010.

[17] E. J. Doedel, B. E. Oldeman, Auto-07P: Continuation and bifurcation software for ordinary differential equations, Tech. rep., Department of Computer Science, Concordia University, Montreal, Canada, available from http://indy.cs.concordia.ca/auto/ (2009).

[18] P. S. Bulson, The stability of flat plates, Chatto & Windus, London, UK, 1970.

[19] J. Becque, The interaction of local and overall buckling of cold-formed stainless steel columns, Ph.D. thesis, School of Civil Engineering, University of Sydney, Sydney, Australia (2008).

[20] E. L. Liu, M. A. Wadee, Mode interaction of global and local buckling in thin-walled I-section struts with rigid flange–web joints, in: D. Camotim, P. B. Dinis, S. L. Chan, C. M. Wang, R. Gonçalves, N. Silverstre, C. Basaglia, A. Landesmann, R. Bebiano (Eds.), Proceedings of ICASS 2015, 2015, paper number: 42.

[21] G. W. Hunt, M. A. Wadee, Localization and mode interaction in sandwich structures., Proc. R. Soc. A 454 (1972) (1998) 1197–1216. doi:10.1098/rspa.1998.0202.

[22] M. K. Wadee, G. W. Hunt, A. I. M. Whiting, Asymptotic and Rayleigh–Ritz routes to localized buckling solutions in an elastic instability problem, Proc. R. Soc. A 453 (1965) (1997) 2085–2107. doi:10.1098/rspa.1997.0112.

[23] L. Bai, M. A. Wadee, Imperfection sensitivity in thin-walled I-section struts susceptible to cellular buckling, Int. J. Mech. Sci. 104 (2015) 162–173. doi:10.1016/j.ijmecsci.2015.10.010.

[24] M. A. Wadee, Effects of periodic and localized imperfections on struts on nonlinear foundations and compression sandwich panels, Int. J. Solids Struct. 37 (8) (2000) 1191–1209. doi:10.1016/S0020-7683(98)00280-7.

[25] S. P. Timoshenko, J. M. Gere, Theory of elastic stability, McGraw-Hill, New York, USA, 1961.

[26] M. B. Monagan, K. O. Geddes, K. M. Heal, G. Labahn, S. M. Vorkoetter, J. McCarron, P. DeMarco, Maple 10 Programming Guide, Maplesoft, Waterloo ON, Canada, 2005.

[27] N. S. Trahair, M. A. Bradford, D. A. Nethercot, L. Gardner, The behaviour and design of steel structures to EC3, 4th Edition, Taylor & Francis, 2008.

[28] D. Dubina, V. Ungureanu, R. Landolfo (Eds.), Design of cold-formed steel structures, Wiley-Blackwell, 2012. doi:10.1002/9783433602256.

[29] D. Saito, M. A. Wadee, Numerical studies of interactive buckling in prestressed steel stayed columns, Eng. Struct. 31(1) (2009) 1–15. doi:10.1016/j.engstruct.2008.09.008.

[30] C. J. Budd, G. W. Hunt, R. Kuske, Asymptotics of cellular buckling close to the Maxwell load, Proc. R. Soc. A 457 (2016) (2001) 2935–2964. doi:10.1098/rspa.2001.0843.

[31] ABAQUS, Version 6.14, Dassault Systèmes, Providence, USA, 2014.